Investigation of Enhanced Heat Transfer in Hollow Blade by Diamond-inspired Structure for Dehumidification in Steam Turbine

Yan Pin[a **], Xiaoyuan Wen[b **], Xiaodan Hu[b], Shuo Cheng[a], QI Shun[a], Zhuhai Zhong[a], Pengfei Han[d], Cun Wang[b], Wei Jiang[bc *]

State Key Laboratory of Clean and Efficient Turbomachinery Power Equipment , Deyang 618000, China.

a Dongfang Electric Corporation Dongfang Turbine Co.,LTD, Deyang 618000, China.

b Key Laboratory of Hydraulic Machinery Transients (MOE), Wuhan University, Wuhan, Hubei Province, China.

c Suzhou Institute of Wuhan University, Suzhou, Jiangsu Province, China.

d Rundian Energy Science and Technology Co., LTD, Zhengzhou, Henan Province, China.

*Corresponding author, jiangwei@whu.edu.cn.

** The two authors have the same contribution to this study.

Abstract

Wet steam erosion plays a pivotal role in influencing the efficient and safe operation of steam turbines. The dehumidification technique, which combines hollow blade heating and purging, exhibits significant performance in the low-pressure, long-blade stages. However, the hollow structure has a pronounced impact on blade strength and often results in low heat transfer efficiency. In this study, we introduce a turbulence generator inspired by the diamond lattice bonding to modify the internal channel structure of hollow long blades. This diamond-inspired structure aims to enhance turbulence within the blades, thereby increasing surface area and heat transfer coefficients, ultimately reducing erosion caused by secondary water droplets on downstream blades. Our findings indicate that incorporating a diamond-inspired structure as a framework within the conventional slot cavity blades results in a notable temperature increase on the blade surfaces. Specifically, at 100% rated flow conditions, the average blade surface temperature rises from 352K to 357K. The diamond-inspired structure enhances heat transfer without significantly compromising the blades' power output. Furthermore, reducing the bond length from 30mm to 20mm leads to an additional temperature increase from 357K to 359K. This suggests that a denser diamond lattice structure is more favorable for heating the stator blades.

Keywords: *Heat transfer; Dehumidification; Steam turbine; Diamond-inspired Structure*

1. Introduction

The issue of wet steam erosion has consistently been a critical factor affecting the safe and efficient operation of steam turbines, with particular prominence in the context of high-power steam turbines featuring long blades. On one hand, the presence of large droplets (secondary droplets) in wet steam can lead to erosion on the turbine blades as shown in Figure 1 [1]. On the other hand, wet steam introduces wetness losses: approximately 1% moisture corresponds to a 1% reduction in efficiency. This impact is especially severe in high-power nuclear steam turbines, where wet steam significantly impairs operational efficiency. As the proportion of renewable energy sources in the power grid increases, the demand for load regulation capability in steam turbine units also grows. Consequently, ensuring the high efficiency and safety of high-power steam turbines operating at partial load conditions [2, 3] has become a focal point of research internationally.

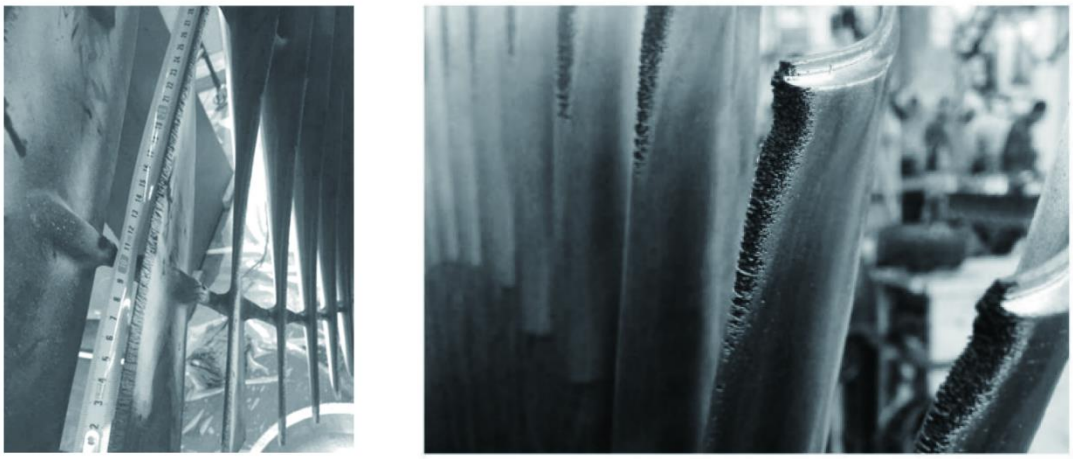

Figure 1. Serious water erosion of last-stage blade of low-pressure rotor.

In the realm of two-phase wet steam flow within steam turbines, extensive research have been conducted. Building upon the Oswatitsch nucleation theory, Gyarmathy [4] formulated a calculation formula for droplet growth rates at high Knudsen numbers. Kirillov [5] established equations describing the motion of water films on flat blade surfaces. Williams et al. [6-8] extended Kirillov's methods to three-dimensional blade surfaces. Arimi [7-9] delved into the relationship between droplet surface tension and droplet radius growth, as well as the characteristics of liquid film shear forces. Young and White [9] expanded wet steam research into the low-pressure stages of steam turbines. Xinggang Yu et al. [10-13] investigated the characteristics of wet steam condensation flow and, combining theory with numerical methods, derived wetness loss coefficients for low-pressure stages. Li Liang [14], through coupled calculations of water vapor and water film, examined factors influencing wall film distribution. Guojie Zhang et al.[15] introduced NaCl particle injection in wet steam, and found that the nucleation rate and droplet production is reduced by heterogeneous condensation. These research endeavors have laid essential theoretical foundations for addressing the issue of wet steam erosion on steam turbine blades.

In this context, the dehumidification technology for long blade stages under harsh operating conditions has consistently remained a research focal point. Existing dehumidification techniques can be classified into three categories based on the location of the dehumidification structure: diaphragm dehumidification, moving-blade dehumidification, and stator blade dehumidification[16,17].

Diaphragm dehumidification, while effective for conventional blade stages with separation factors not exceeding 15% [18], tends to yield less satisfactory dehumidification results and is less suitable for long blade stages in high-power steam turbines. Moving-blade dehumidification involves creating water removal channels on the surfaces of rotor blades. While it significantly impacts the strength of rotor blades, it is not applicable to long blade stages in high-power steam turbines and is presently only employed in the high-pressure stages of nuclear power turbines. stator blade dehumidification, based on the hollow stator blade structure, employs methods such as suction, purging, and heating to eliminate water films deposited on the blade surfaces. It can be further divided into two specific methods: suction slot dehumidification and heating-purging dehumidification.

Suction slot dehumidification involves drawing in and expelling water films through slots created on the stator blade surfaces. However, the dehumidification effectiveness is constrained by various factors affecting the suction capacity of the stator blade cavities, and therefore, the results are not entirely satisfactory [19, 20]. Heating-purging dehumidification introduces high-temperature steam from the upstream into the hollow stator blades, and heats the blade surfaces to evaporate the surface water films, creating non-wetting characteristics on the blade surfaces [21-24]. Subsequently, these films are expelled through slots at the trailing edge, breaking up large water droplets formed as a result of the tearing of water films at the trailing edge [25-29]. This approach exhibits a more pronounced dehumidification effect. However, for high-power steam turbines with long blades, further research is required on the heat transfer enhancement, flow characteristics, and applicability of heating-purging methods.

Conventional hollow stator blades suffer from limited heat transfer efficiency within their internal cavity channels and face challenges in maintaining adequate blade strength due to the constraints of the cavity structure. Existing research efforts have mostly focused on improving hollow blade designs based on traditional manufacturing processes, with optimization strategies often limited to the incorporation of rib structures and similar modifications[30]. However, these attempts have shown limited effectiveness in enhancing both heat transfer efficiency and blade strength. In recent years, the field of biomimicry has gained significant traction in various domains. Within the trend of interdisciplinary research, the scope of biomimetic studies has expanded from initially imitating biological organisms to simulating all useful information from the natural world, environments, and life that cater to human needs. Previous research has also indicated the advantages of biomimetic blades in controlling separation flows [31, 32]. Diamond, as one of the hardest naturally occurring substances in the world, possesses a crystal lattice structure where carbon atoms form tetrahedral bonds with each other, creating an infinite three-dimensional framework [33-35]. In this study, we aim to apply biomimetic principles by devising an original high-surface area and high-strength topological structure as an internal channel within hollow long blades. We emulate the tetrahedral topology of diamond's structure to create periodic topological structural units [36], which will be integrated into the internal channels of the hollow long blades.

Given the distinct flow-disrupting effects of the tetrahedral topology inspired by diamond, it can significantly enhance the heat transfer efficiency between the heated steam and the blade surfaces. This, in turn, raises the surface temperature of the hollow blades. In the heating-purging structure of the hollow stator blades, steam expelled from the trailing edges of these hollow blades can be utilized to adjust the direction of the main steam flow. This innovative approach can address the issue of wet steam erosion, and ultimately boosting blade efficiency and safety.

2. Research Methodology

2.1 Non-Equilibrium Steam Condensation Flow Model

The non-equilibrium steam condensation flow model is employed to simulate the condensation state of steam when it is confined by free energy barriers during the expansion process. In the ANSYS CFX, the homogeneous nucleation model is based on classical nucleation theory. When the droplet diameter is relatively small, the droplets can effectively follow the motion of steam, and the slip velocity between steam and droplets can be neglected, assuming that both the droplets and steam share the same velocity field.

In the non-equilibrium steam condensation flow model, the vapor phase is treated as the continuous phase, while the liquid phase resulting from condensation is treated as the dispersed phase. The continuity equations for the non-equilibrium steam condensation flow model are as follows:

Vapor Phase:

$$\frac{\partial(\rho_c r_c)}{\partial t}+\frac{\partial(\rho_c u_i r_c)}{x_i}=-(S_d+m\cdot r_c J) \quad (1)$$

Liquid Phase:

$$\frac{\partial(\rho_d r_d)}{\partial t}+\frac{\partial(\rho_d u_i r_d)}{x_i}=(S_d+m\cdot r_c J) \quad (2)$$

where, $m\cdot r_c J$ denotes the mass source term for newly nucleated liquid droplets.

J is the nucleation model, defined as the number of droplets produced in a unit volume of steam per unit time, and its expression is as follows:

$$J=q_c S_d\left(\frac{2\sigma}{\pi M_w{}^3}\right)^{\frac{1}{2}}\frac{\rho_c}{\rho_d}exp\left(-\frac{4\pi R_d^{*2}\sigma}{3k_b T_c}\right) \quad (3)$$

R_d^* represents critical radius and its expression as follows:

$$R_d^*=\frac{2\sigma T_s}{\rho_d H_{lat}(T_s-T_c)} \quad (4)$$

$$H_{lat}=H_c-H_d \quad (5)$$

S_d represents the mass source term resulting from condensation on pre-existing liquid droplet cores and can be calculated as follows:

$$S_d=\rho_d\frac{3r_d}{R_d}\frac{dR_d}{dt} \quad (6)$$

The term $m\cdot r_c J$ and S_d together constitute the mass source term. In the case of evaporation, its value is negative, whereas, in the case of condensation, its value is positive.

The model used in the above formula is Young's growth law proposed by Young, JB, and he proposes two correction coefficients α and β. α is the growth factor and relates the condensation coefficient to the evaporation coefficient, and β is used to measure the distance from the droplet when the continuous process occurs. The corrected expression as follows:

$$\frac{dR_d}{dt}=\frac{\lambda_c(T_s-T_c)(1-R_d{}^*/R_d)}{H_{lat}R_d\rho_d\left[\frac{1}{1+2\beta \mathrm{K_n}}+3.78(1-v)\frac{K_n}{Pr_c}\right]} \quad (7)$$

$$K_n = 1.5\frac{\mu_c\sqrt{RT_c}}{2R_d p} \quad (8)$$

$$v = \frac{RT_s}{H_{lat}}[\alpha - 0.5 - \frac{2-q_c}{2q_c}(\frac{\gamma+1}{2\gamma})(\frac{C_{p,c}T_s}{H_{lat}})] \quad (9)$$

$$Pr_c = \frac{\mu_c C_{p,c}}{\lambda_c} \quad (10)$$

The momentum equations for the vapor and liquid phases in the non-equilibrium steam condensation flow model use the same equation and can be expressed as:

$$\frac{\partial(\rho_c u_i)}{\partial t} + \frac{\partial(\rho_c u_i u_j)}{x_i} = -\frac{\partial P}{\partial x_j} + \frac{\partial \tau_{ij}}{x_i} \quad (11)$$

For compressible fluids, the energy conservation equation is expressed in terms of total enthalpy. Therefore, for the vapor phase in the non-equilibrium steam condensation flow model, the energy conservation equation takes the following form:

$$\frac{\partial r_c(\rho_c h_{totc} - P)}{\partial t} + \frac{\partial(r_c\rho_c u_i h_{totc})}{x_i} = \frac{\partial}{x_i}\left(r_c\lambda_c\frac{\partial T_c}{\partial x_i}\right) + \frac{\partial(r_c u_i h_{ij})}{x_i} - \dot{S}h_{totd} + \frac{3r_d Q_d}{R} \quad (12)$$

where h_{ij} represents the energy exchange between the vapor phase and the liquid phase in the mass transfer process reflected in the energy conservation equation.

There are two kinds of energy transport equations for liquid phase, one is for large droplets, and the treatment method is based on the temperature phase transformation model through the conservation equation of droplet enthalpy. For another class of smaller droplets, the description is based on the microdroplet heat transfer model, and the expression of droplet temperature is as follows:

$$t_1 = t_s(p) - \Delta t\frac{R_d{}^*}{R_d} \quad (13)$$

In addition, when calculating the heat transfer area between the steam and the droplet, in addition to the droplet diameter, the parameter of the number of droplets is also needed. The number of droplets is calculated by the quantity conservation equation, whose expression is as follows:

$$\frac{\partial\rho_d N}{\partial t} + \frac{\partial(\rho_d u_i N)}{\partial x_i} = \rho_d r_d J \quad (14)$$

The vapor phase volume fraction r_c and liquid phase volume fraction r_d in the above expression meet the following formula:

$$r_c + \sum_1^{nd} r_d = 1 \quad (15)$$

where *nd* represents the number of liquid phase.

Based on classical nucleation theory and droplet growth formula, the non-equilibrium phase transformation model is suitable for the numerical calculation of the spontaneous condensation process of susaturated steam, including the initial condensation flow field and the law of droplet deposition. The E-E two-phase flow model is used to calculate the initial condensation, while the E-L model is used to calculate the droplet deposition.

2.2 Turbulence Model

This work conducts a numerical simulation study of the flow characteristics inside a steam turbine by solving the N-S equations. To make the equations solvable, it is essential to employ an appropriate turbulence model. The flow within a steam turbine is highly intricate, featuring strong three-dimensional flow patterns. Specifically, the low-load flow regime, a focus of this work, exhibits significant adverse pressure gradients on the blade suction side, leading to flow separation. The k-ω SST turbulence model is well-suited for simulating flow separation caused by adverse pressure gradients and has found widespread application in the field of numerical flow simulations within steam turbines. Consequently, this paper utilizes the k-ω SST turbulence model to address the turbulence aspects of the flow.

The k-ω SST turbulence model imposes stringent requirements on the quality of wall grid cells, aiming to avoid y+ values less than 1, which can be challenging to achieve for low-pressure turbine blades. However, in ANSYS CFX, the k-ω SST turbulence model is combined with an automatic wall function, which allows for accurate simulations of the flow field near the walls of low-pressure steam turbine blades.

2.3 Model Establishment and Mesh Generation

To investigate the heat transfer characteristics of a low-pressure stage in a steam turbine, a three-dimensional model, as shown in Figure 2, was constructed. Considering that the turbine blades are arranged in a rotating periodic manner around an axis, this study employed two stages with only single stator and rotor blade as the computational domain. Non-structured meshes were used to accommodate the twisted structure of the blades in the low-pressure stage. In our study, the diamond-inspired structure consists of periodically repeated units. During the generation of the unstructured mesh, the target element size was set to 12 mm. On average, each unit contains approximately 27,423 cells and 6,374 nodes, ensuring a high level of accuracy in the geometric and mechanical representation. However, during the coupling process between the periodic structure and the blade structure, some units become incomplete due to geometric interactions. This results in the inability to derive an exact integer number of units. Such discrepancies are typical in meshing complex coupled structures, where boundary regions cause units to be partially formed, and the resulting mesh is illustrated in Figure 2. To better simulate the flow conditions within the boundary layer, an O-mesh was applied to the blade surfaces, with boundary layer refinement. Additionally, mesh refinement was applied to the blade tip section, root section, leading edge, and trailing edge.

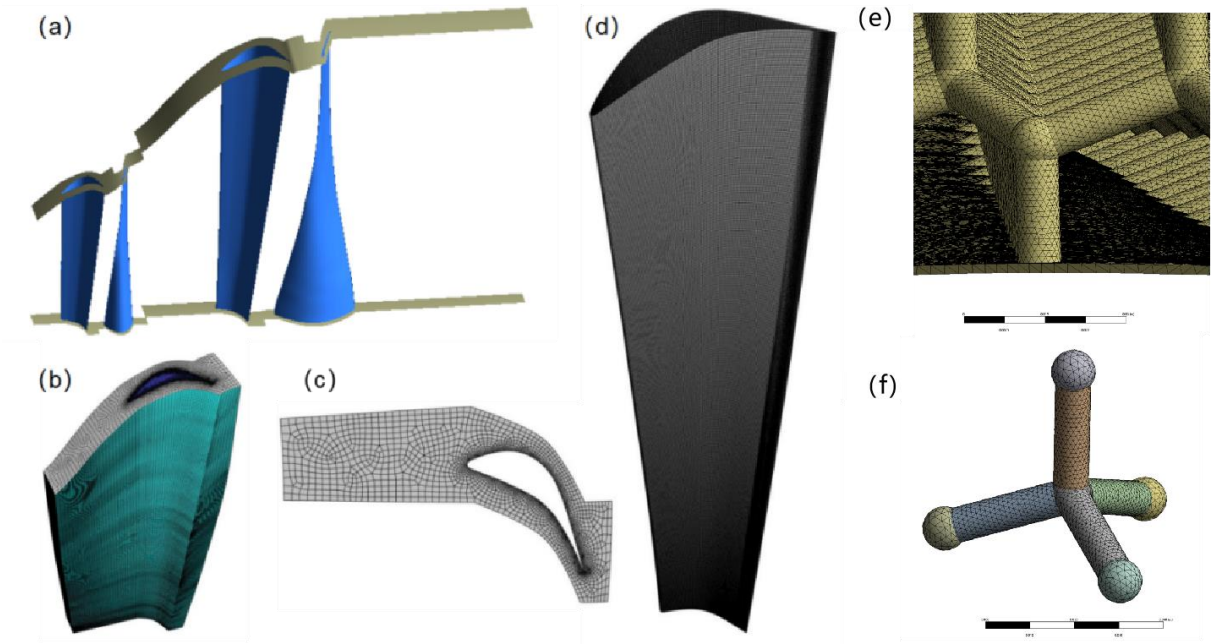

Figure 2. Physical Model and Mesh Details Physical Model of the Last Two Stages of a Wet Steam Turbine. (a) Physical Model. (b) Cascade Mesh. (c) Sectional Mesh. (d) Blade Mesh.(e) Unstructured grid. (f) Diamond-inspired structure.

To eliminate the influence of mesh resolution on the computational results, a mesh independence validation was first conducted for the last stage. The computational boundary conditions employed for validation were as follows: inlet total pressure of 0.017 MPa, inlet total temperature of 329.8 K, inlet gas fraction of 0.87, and outlet back pressure of 5.4 kPa. Three different mesh densities were used, as summarized in Table 1. It is important to note that the alteration of mesh node numbers did not affect the mesh topology of the blades and the height of the first layer of cells near the blade surfaces.

Figure 3 presents the variation in steam subcooling along the rotor blade passage (Figure 3a) and the distribution of surface pressure on the rotor blade (Figure 3b). In the wet steam nonequilibrium condensation flow model, as steam expands to the saturation temperature, condensation does not occur immediately due to the constraints of free energy. Instead, a certain degree of subcooling is required before condensation takes place. Therefore, subcooling is a critical parameter for non-equilibrium steam condensation. As shown in Figure 3(a), Mesh 2 simulates the variation in subcooling along the rotor blade passage, which is consistent with the trend observed for Mesh 3. Importantly, Mesh 2 yields the same subcooling peak and its corresponding location. Additionally, for this operating condition, non-equilibrium spontaneous steam condensation occurs near the trailing edge of the rotor blade. Figure 3(b) demonstrates that Mesh 2 captures the pressure spike on the back-pressure side near the trailing edge, resulting from non-equilibrium condensation, just as Mesh 3 does. Consequently, the density of Mesh 2 meets the computational requirements of this study.

Table 1. Mesh Nodes and Cell Volumes

Mesh Number	Nodes	Cell Volumes
1	412603	1480171
2	652205	2350066
3	1133361	4039754

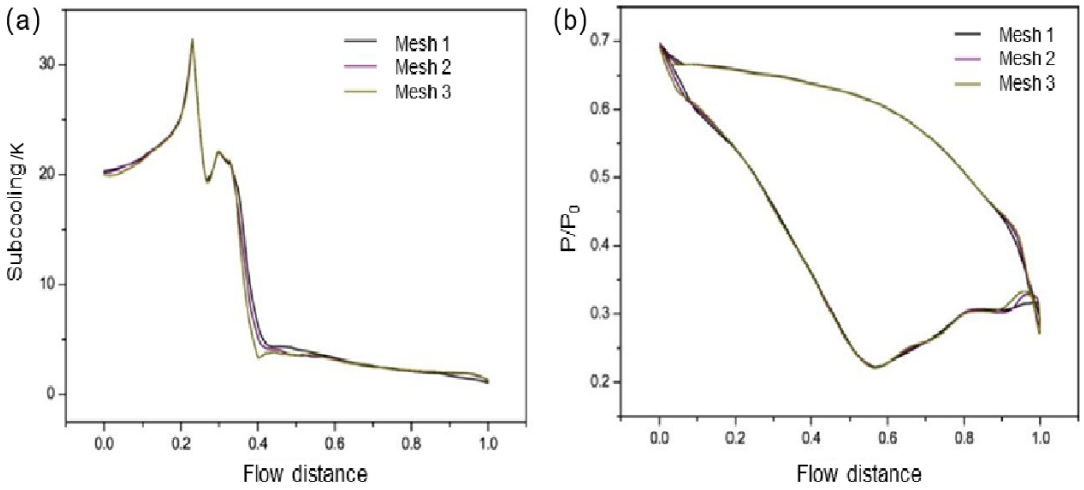

Figure 3. Steam Non-Equilibrium Condensation Flow Subcooling (a) and Blade Surface Pressure Distribution (b)

2.4 Numerical Model Validation

This study employs a steam non-equilibrium spontaneous condensation model based on the dual Euler approach to compute the flow characteristics of wet steam in the low-pressure last stage. To validate the accuracy of this numerical model for simulating steam non-equilibrium spontaneous condensation flow, computations are initially conducted on the Laval nozzle and the Bahktar cascade.

The Laval nozzle [37] exhibits an expansion ratio that is close to that found in actual steam turbines, making it a suitable choice for researching the flow characteristics of spontaneously condensing steam. In this study, Laval A nozzle is analyzed, with a throat height of 63 mm and an outlet height of 114 mm. Figure 4 illustrates the nozzle geometry, numerical simulation results and measurements, comparing the pressure distribution and water droplet diameter distribution along the centerline of Laval Nozzle A. The figure shows that the predicted droplet diameters of steam in the nozzle are of the same order of magnitude as the experimental value, although the simulation results are approximately 20% lower. This discrepancy is mainly due to the averaging process used in the calculations. On the other hand, the pressure distribution within the nozzle aligns well with the experimental data, with the trends in pressure changes and the location of the condensation shock wave accurately corresponding.

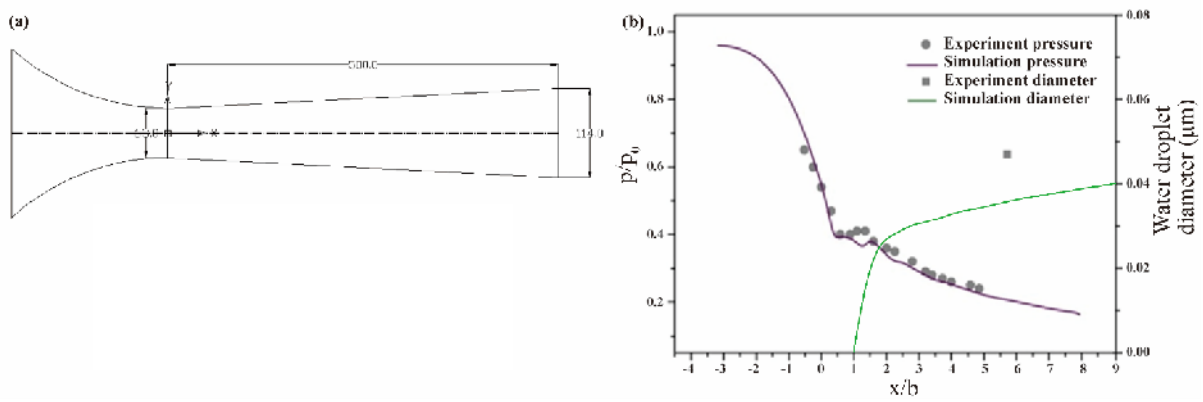

Table 2. Boundary conditions on inlet and outlet

Parameter	Value
Inlet total pressure	25kPa
Inlet total temperature	354.6K
Outlet boundary	Supersonic

Figure 4. Laval nozzle A validation results. (a) Experiment boundary conditions and geometric parameters of Laval nozzle A. (b) Pressure and water droplet distribution along the centerline in Laval nozzle A.

In conclusion, the non-equilibrium spontaneous condensation model used in this study effectively captures the pressure spikes resulting from spontaneous steam condensation and accurately simulates pressure distribution and water droplet size within the Laval nozzle.

2.5 Boundary Conditions

This study considers two different operating conditions: 100% rated flow and 50% rated flow. Figure 5 presents a schematic diagram of the traditional stator blade cavity structure. Heated steam enters the cavity from the top of the stator blade and exits through the clearance at the trailing edge of the blade, mixing with the main steam flow. The cavity boundary conditions for the 100% rated flow condition are as follows: inlet total temperature 370 K, inlet humidity 0, outlet static pressure 5.4 kPa, and inlet flow rate of 0.16 kg/s. The boundary conditions for the 50% rated flow condition are as follows: inlet total temperature 370 K, inlet humidity 0, outlet static pressure 5.4 kPa, and inlet flow rate of 0.08 kg/s.

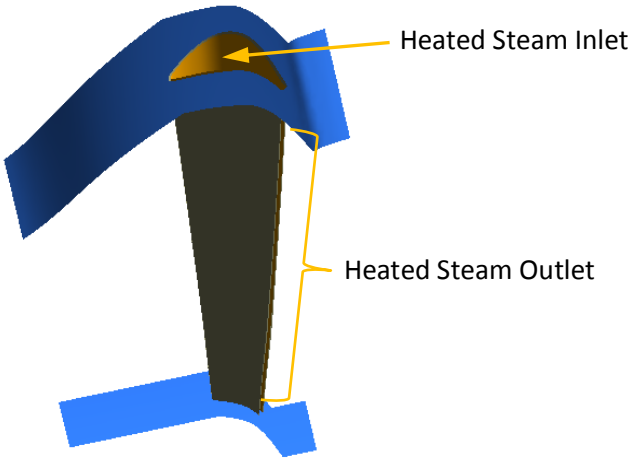

Figure 5. Boundary Conditions for the stator blade Cavity Structure

3. Results and Discussion

3.1 Performance of Traditional Single-Slot Cavity

This study initiated with an investigation of the heating performance of traditional single-slot cavity. This was used as the comparative baseline for the subsequent optimization structures.

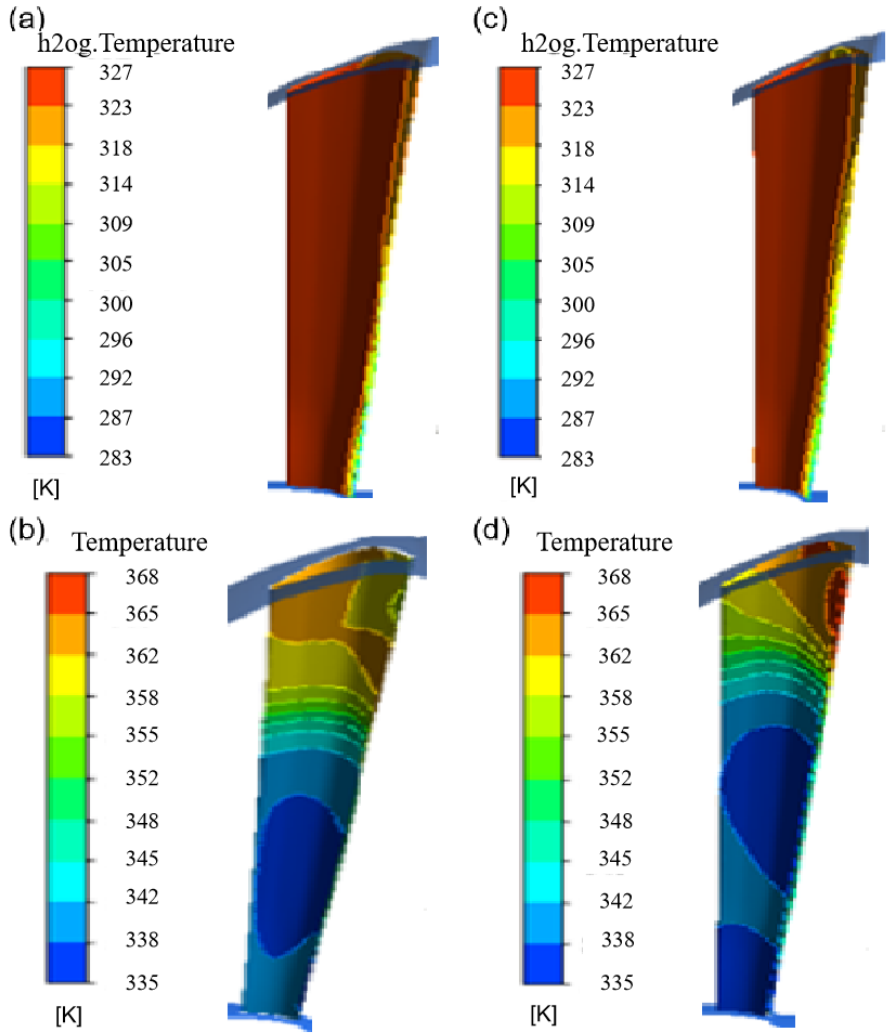

Figure 6. Surface Temperature Distribution of Conventional and Cavity Blades. (a) Conventional blade at 100% Rated Load. (b) Cavity blade at 100% Rated Load. (c) Conventional Blade at 50% Rated Load. (d) Cavity Blade at 50% Rated Load.

Figure 6 shows the surface temperature distribution of the last-stage blades under 100% and 50% rated flow conditions for both the conventional blade design (without steam heating) and the cavity blade design. It can be observed from the figure that the introduction of heating steam significantly raises the surface temperature of the stator blades, with a more pronounced temperature increase closer to the heating steam inlet. The above temperature statistics method adopts the area average method, and its formula is as follows:

$$\bar{T} = \frac{\sum_{i=1}^{n} T_i \Delta S_i}{S} \quad (16)$$

The statistical results indicate that with the introduction of heating steam, the average surface temperature of the last-stage stator blades increases from 332K to 348K, which is a 16K rise under 100% rated flow. The heating effect of the same relative mass flow of heating steam increases the temperature of the last-stage stator blades by 21K under 50% rated flow. This suggests that the steam heating method performs even better at low flow rates, indicating its good operational adaptability.

The heating steam is discharged from the trailing edge gap of the blades after heating the stator blades. Its direction and magnitude of discharge may not align with the direction and magnitude of the mainstream flow, resulting in mixing losses. Therefore, Figure 7 illustrates streamline diagrams for both the conventional and cavity blade designs at 100% rated flow conditions. It is evident from the figure that in both cases, the flow remains predominantly near the blade surfaces, and the influence of the heating steam on the mainstream flow is not significant.

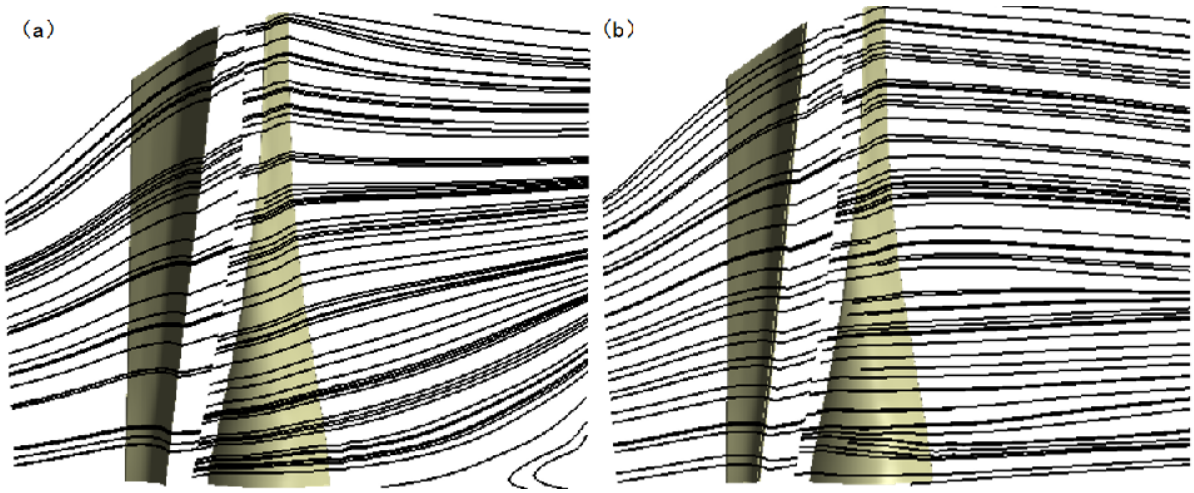

Figure 7. Streamline Diagrams of Conventional and Cavity Blades at 100% Rated Flow Conditions. (a) Conventional Blade. (b) Cavity Blade.

3.2 Performance of Optimized Double-Slot Cavity

In the traditional single-slot cavity heating method, the stator blades are heated. Inspired by moisture-removal groove structure, this section introduces a double-slot cavity blade design, as depicted in Figure 8(a). In this configuration, purging steam exits through two slots in the blade body rather than from the trailing edge. The water film deposited in front of the slots is lifted and separated from the blade surface by the purging steam, effectively reducing or preventing water droplet deposition on the blade surface, thereby achieving a dehumidification effect.

Figure 8(c) presents the temperature distribution on the surface of the rotor blade with double-slot cavity at 100% rated flow conditions. A comparison with Figure 6 reveals that the double-slot cavity blade design exhibits a 21 K increase in the highest temperature, a 17 K decrease in the lowest temperature, and a 1 K increase in average temperature, rising from 348 K to 349 K. Furthermore, the high-temperature region has shifted from the trailing edge to the middle of the blade. This shift can be attributed to the lack of convective heat exchange at the trailing edge of the double-slot cavity, where no heating steam is purged. Besides, Figures 8(c) illustrate the presence of a large, unheated low-temperature region downstream of the slot.

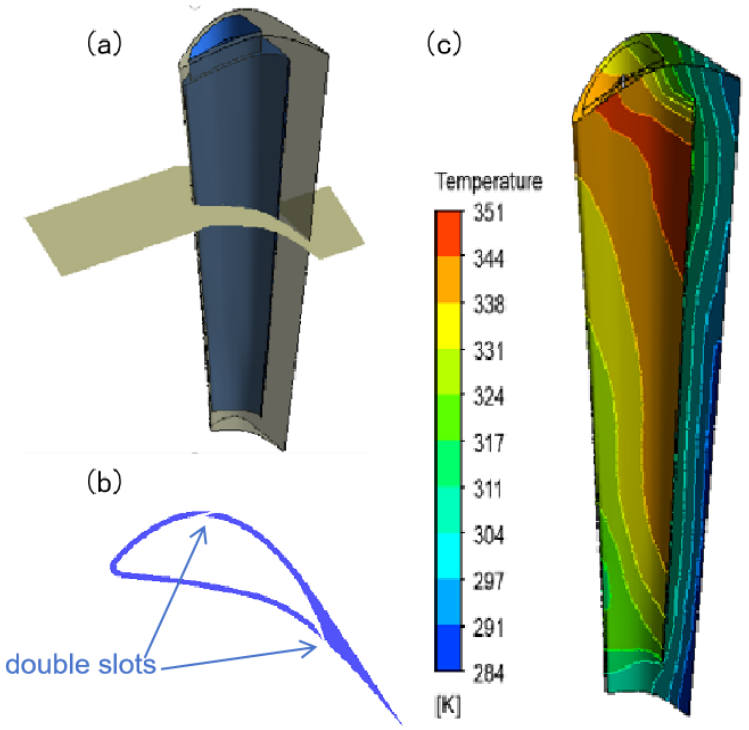

Figure 8. Double-Slot Cavity Blade Structure and Its Surface Temperature Distribution. (a) stator blade. (b) stator blade Cross-Section. (c) surface temperature distribution.**Error! Reference source not found.**The influence of the trailing edge slot on the aerodynamic forces on the blade can be observed through the analysis of the aerodynamic moments. The statistical results of the blade aerodynamic moments are as follows: at 100% rated flow conditions, the aerodynamic moment for the double-slot cavity configuration on the downstream blade is 799 Nm, for the conventional configuration, it is 739 Nm, and for the trailing edge slot configuration, it is 634 Nm. At 50% rated flow conditions, the aerodynamic moment for the double-slot cavity configuration on the downstream blade is 237 Nm, for the conventional blade, it is 210 Nm. The trailing edge slot structure results in a decrease of 6.5% in the aerodynamic moment and power output, while the double-slot cavity configuration leads to an increase of 4.1%. This indicates that the power potential of the 5% heating steam is partially recovered downstream.

Figure 9 provides a further comparison of the surface humidity of the stator blade for the conventional configuration and the double-slot cavity configuration at 100% rated flow conditions. It is evident that the heating effect of the steam not only increases the surface temperature of the blade but also reduces the surface humidity. This reduction in humidity is particularly significant downstream of the slots. The statistical results show that at 100% rated flow conditions, the average surface humidity of the double-slot cavity configuration is 3.7% relative to 3.9% for the conventional configuration, representing a 5% decrease. It is important to note that the reduction in humidity does not fully capture the dehumidification effect. In practice, the liquid film is in direct contact with the wall surface, and its thermal conductivity is significantly higher than that of the moist steam.

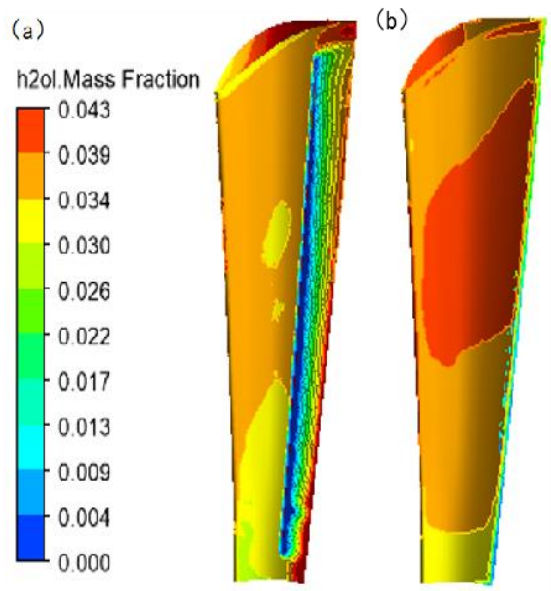

Figure 9. Steam Humidity on the Last-Stage stator blade Surfaces of Conventional Blades and Double-Slot Cavity Blades Under Various Conditions. (a) Double-slot Cavity Configuration , 100%. (b) Conventional Configuration, 100%.

Building upon the aforementioned findings, this work further optimized the angles and positions of the slots in the double-slot cavity blade. The blade profiles before and after optimization are presented in Figure 10 (a) and (b). The slots on both the pressure and suction sides were shifted downstream, aligning the exhaust direction of the pressure-side slots more closely with the trailing edge of the balde profile. The impact of slot optimization on the blade's surface temperature distribution is demonstrated in Figure 10 (c) and (d). A comparison reveals that moving the slots backward significantly reduces the low-temperature area downstream of the pressure-side slots and considerably expands the high-temperature region upstream. After optimization, the average surface temperature of the airfoil increased from 349 K to 352 K, representing a 3 K increase.

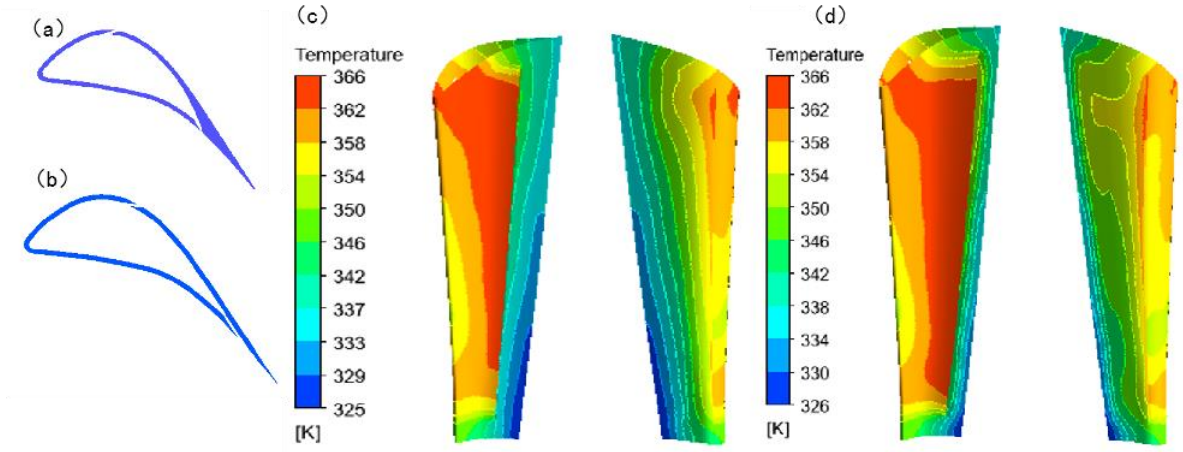

Figure 10. Comparison of Last-Stage stator blade Surface Temperature Distribution of Double-Slot Cavity Blades Before and After Slot Optimization. (a) Blade Section Before Optimization. (b) Blade Section After Optimization. (c) Temperature Distribution Before Optimization. (d) Temperature Distribution After Optimization.

3.3 Diamond-inspired Structure

The presence of vortices in cavity structures is unavoidable, leading to the emergence of low-temperature regions. Additionally, cavity structures can affect the structural strength of the blade, necessitating thicker blade wall to meet the strength requirements. In this study, a mesoscale diamond-inspired bonding pattern, as depicted in Figure 11, is employed as the channel structure within the blade. The structure strengthens internal flow disruption, increasing the heat transfer coefficient and surface area to improve heat transfer efficiency. Figure 12(a-d) provides a comparison of the heat flux density and turbulence intensity on the inner surfaces of the diamond-inspired cavity and the double-slot cavity. Evidently, the diamond-inspired structure enhances turbulence intensity and heat flux density on the cavity walls.

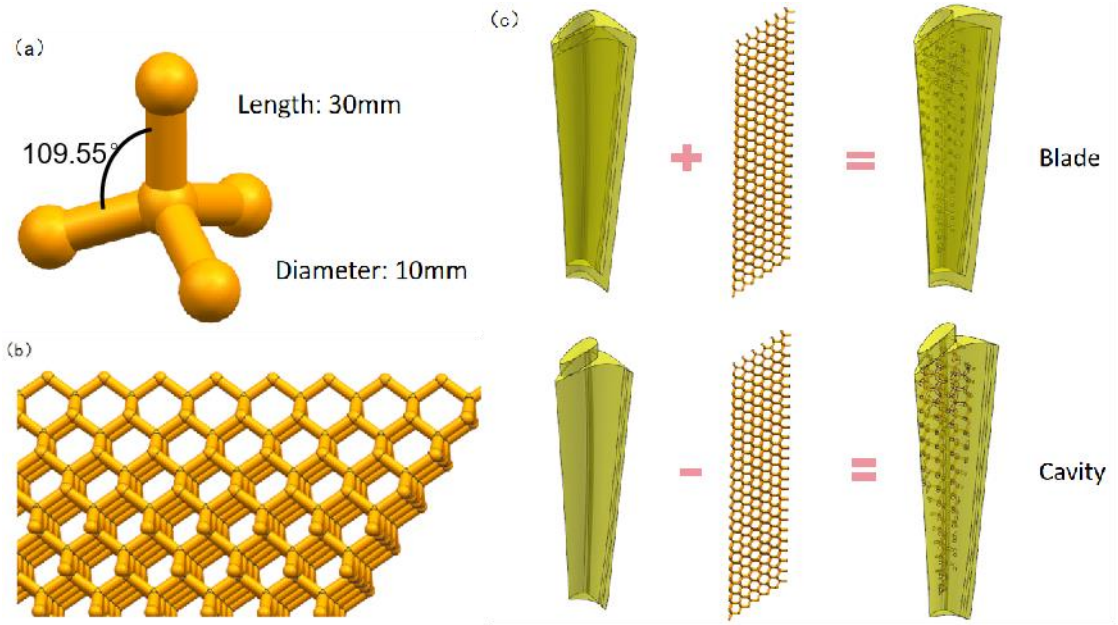

Figure 11. Schematic of the diamond-inspired Structure. (a) Diamond-inspired Unit Size. (b) Diamond-inspired Topology. (c) Diamond-inspired Blade and Cavity Channel.

The increase in turbulent intensity and thermal flux density directly results in elevated surface temperatures of the blades. As shown in Figure 12(e-f), the inclusion of the diamond-inspired structure raises the average temperature from 352K to 357K at 100% rated flow conditions, an increase of 5K. Compared to double-slot cavity blades, the diamond-inspired cavity's high-temperature region concentrates in the upper half of the blade. Considering the fact that much more water droplet is deposited in the upper half of the blade, the temperature distribution of the diamond-inspired cavity aligns better with the water droplet deposition rate distribution. Clearly, the temperature distribution of the diamond-inspired cavity is more favorable for heating and evaporating the water film on the blade surface.

Additionally, this work compared the moments of the diamond-inspired cavity blades and double-slot cavity blades. At 100% rated flow conditions, the moments for the diamond-inspired blades and cavity blades were 800 Nm and 801 Nm, respectively. The inclusion of the diamond framework did not affect the blades' performance in terms of power output.

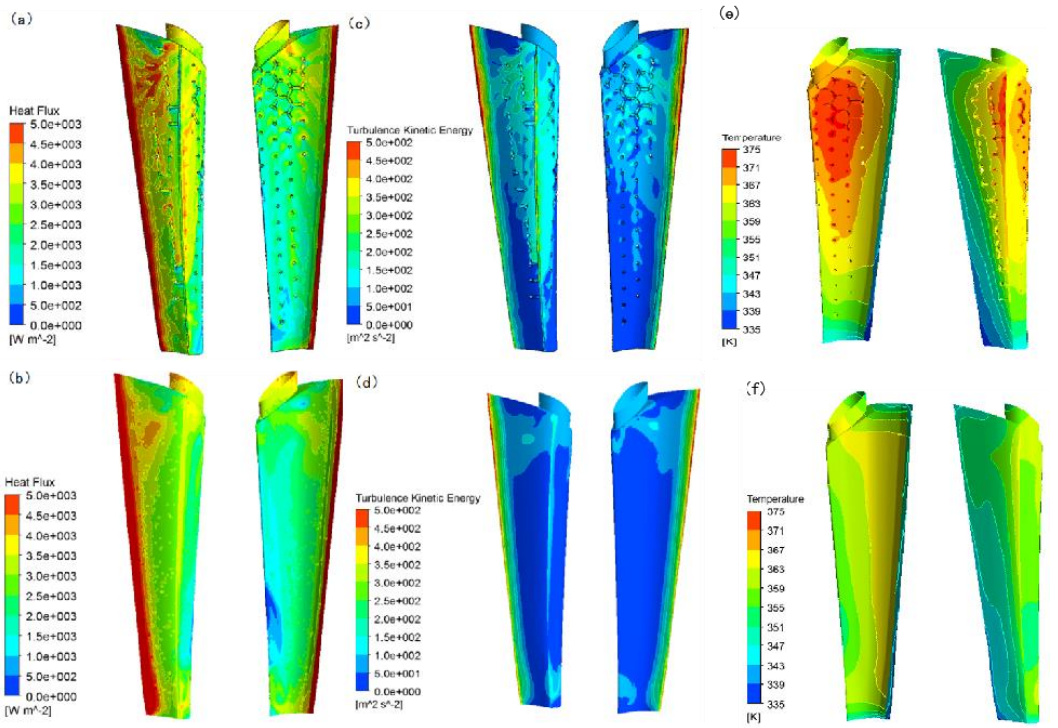

Figure 12. Comparison of Thermal Flux Density, Turbulent Kinetic Energy and Temperature Distribution on the Inner Surfaces of Diamond-inspired Cavity and Double-Slot Cavity. (a) Thermal Flux Density of Diamond-inspired Cavity. (b) Thermal Flux Density of Double-Slot Cavity. (c) Turbulent Kinetic Energy of Diamond-inspired Cavity. (d) Turbulent Kinetic Energy of Double-Slot Cavity. (e)Temperature Distribution of Diamond-inspired Cavity. (f) Temperature Distribution of Double-Slot Cavity.

Furthermore, this work revealed that the heating effectiveness of the diamond-inspired cavity structure is primarily related to the length of the diamond structure's bonds. We compared the heating effects of two structures with different bond lengths, as shown in Figure 13(a-b). When the bond length was reduced from 30 mm to 20 mm, the average surface temperature of the blades increased from 357 K to 359 K. Further reductions in bond length are expected to increase the surface temperature even more.

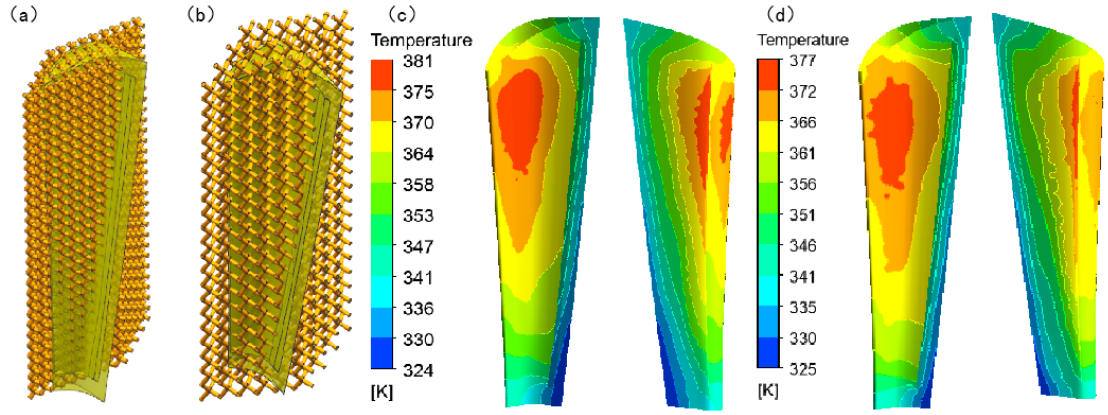

Figure 13. Comparison of Surface Temperature Distribution on the Last-Stage stator blades of diamond-inspired Cavity Blades with Different Bond Lengths. (a) Structure of 20mm Bond Length. (b) Structure of 30mm Bond Length. (c) Temperature Distribution of 20mm Bond Length. (d) Temperature Distribution of 30mm Bond Length.

4. Conclusion

In this study, we performed numerical simulations of condensing flows of wet steam inside the low-pressure last-stage stator blades of a steam turbine. Our focus was to investigate the effects of various cavity and inner structures on the temperature of the stator blades and the aerodynamic forces acting on the rotor blades. The findings can be summarized as follows:

In comparison to the stator blades without cavities, under 100% rated flow conditions, using a traditional single-gap cavity design increased the average surface temperature of the last-stage stator blades from 332K to 348K, resulting in a 16K temperature rise, while the blade moment decreased from 739Nm to 634Nm. Under 50% rated flow conditions, the same relative mass flow of heating steam led to a 21K temperature increase in the last-stage stator blades.

Compared to the single-slot cavity design, under 100% rated flow conditions, adopting a double-slot cavity stator blade increased the average surface temperature of the last-stage stator blades from 348K to 349K, an increase of 1K. The rotor blade moment increased from 634Nm to 799Nm. The double-slot cavity stator blade exhibited a 5% reduction in average surface humidity. Further optimization of the double-slot cavity stator blade by adjusting the angles and positions of the gaps resulted in a 3K temperature increase, with negligible variations in rotor blade moment.

The introduction of a diamond-inspired structure as a skeleton within the optimized double-slot cavity blade led to a 5K temperature increase under 100% rated flow conditions, from 352K to 357K, with minimal changes in rotor blade moment (800Nm). Reducing the key length from 30mm to 20mm further raised the average temperature from 357K to 359K under 100% rated flow conditions, indicating that a finer diamond-inspired structure is more favorable for heating the stator.

ACKNOWLEDGMENTS

This work was supported by National Natural Science Foundation of China [grant numbers 52306046], Open Fund Project of State Key Laboratory of Clean and Efficient Turbomachinery Power Equipment, and Natural Science Foundation of Jiangsu Province [grant numbers BK20230266]. The numerical simulations in this work have been done on the supercomputing system in the Supercomputing Center of Wuhan University.

Nomenclature

H_{lat} - latent heat, kJ/kg

h_{ij} - Energy exchange between the vapor phase and the liquid phase in the mass transfer process (kJ)

h_{totc} - Total enthalpy of the vapor phase (kJ)

h_{totd} - Total enthalpy of the liquid phase (kJ)

J - Nucleation model, defined as the number of droplets produced per unit volume of steam per unit time ($m^{-3} \cdot s^{-1}$)

k_b - Boltzmann constant (J/K)

M_w - Molar mass of water (kg/mol)

m - Nucleation droplet mass (kg)

N - Number of water droplets per unit volume (m^{-3})

R_d^* - Critical radius (m)
R_d - Droplet radius (m)
r_c - Continuous volume fraction
r_d - Discrete volume fraction
S_d - Liquid phase mass source term
T_c - Vapor phase temperature (K)
T_s - Saturation temperature (K)

Greek letters
γ - Heat capacity ratio
μ_c - Water vapor molecular viscosity (N· s/m^2)
λ_c - Steam thermal conductivity W/(m^2·K)
q_c - Condensing coefficient
ρ_c - Continuous phase density (kg/m^3)
ρ_d - Discrete phase density (kg/m^3)
σ - Surface tension (N/m)
τ_{ij} - Shear stress tensor (Pa)

References

[1] ALIABADI M A F, LAKZIAN E, JAHANGIRI A, KHAZAEI I. Numerical investigation of effects polydispersed droplets on the erosion rate and condensation loss in the wet steam flow in the turbine blade cascade [J]. Applied Thermal Engineering, 2020, 164: 114478.

[2] YANG R, YANG J. Unsteady Aerodynamic Study on Last-stage Long Blades of a Steam Turbine Low-pressure Cylinder [J]. Journal of Power Engineering, 2016, 36(5), 360-364.

[3] QUINTANAR-GAGO D A, NELSON P F, DIAZ-SANCHEZ A, BOLDRICK M S. Assessment of steam turbine blade failure and damage mechanisms using a Bayesian network [J]. Reliability Engineering & System Safety, 2021, 207: 107329.

[4] GYARMATHY G. The spherical droplet in gaseous carrier streams: review and synthesis [J]. Multiphase science and technology, 1982, 1(1-4).

[5] KIRILLOV I I, ÎABLONIK R M. Fundamentals of the theory of turbines operating on wet steam [M]. National Aeronautics and Space Administration, 1970.

[6] WILLIAMS J, YOUNG J B. Movement of deposited water on turbomachinery rotor blade surfaces [J]. 2007.

[7] AMIRI RAD E, NAEEMI S, DAVOODI B. Examining the curvature dependency of surface tension in a nucleating steam flow [J]. Heat and Mass Transfer, 2020, 56(1): 207-17.

[8] AMIRI RAD E, SALIMI M. Investigating the effects of shear rate on the collapse time in a gas–liquid system by lattice Boltzmann [J]. Meccanica, 2017, 52(4): 915-24.

[9] WHITE A, YOUNG J, WALTERS P. Experimental validation of condensing flow theory for a stationary cascade of steam turbine blades [J]. Philosophical Transactions of the Royal Society of London Series A: Mathematical, Physical and Engineering Sciences, 1996, 354(1704): 59-88.

[10] CHEN T, XIE D, XIONG Y, ZHANG H. Interaction between wet steam condensation flow and shock wave in LP stage of steam turbine [J]. Proceedings of the CSEE, 2017, 37(21), 6381-6389.

[11] CHUN W, XIE D, YANGHENG X, XINGGANG Y, CHU N, ZHANG H. Research of temperature characteristics of non-equilibrium condensation in transonic steam flow; proceedings of the Turbo Expo: Power for Land, Sea, and Air, F, 2014 [C]. American Society of Mechanical Engineers.

[12] YU X, XIAO Z, XIE D, WANG C, WANG C. A 3D method to evaluate moisture losses in a low pressure steam turbine: Application to a last stage [J]. International Journal of Heat and Mass Transfer, 2015, 84: 642-52.

[13] YU X, XIE D, WANG C, WANG C, ZHOU Y. Numerical investigation of oscillating flows with nonequilibrium condensation in nozzles [J]. Journal of Propulsion and Power, 2015, 31(3): 837-42.

[14] FAN X, LI L, LI S, ZHANG X. Numerical investigation for coupled flow behavior between gas flow and wall film of flat and turbine stator [J]. Journal of Xi'an Jiaotong University, 2016, 50(11), 7-13.

[15] Zhang G, Wang X, Dykas S, et al. Reduction entropy generation and condensation by NaCl particle injection in wet steam supersonic nozzle[J]. International Journal of Thermal Sciences, 2022, 171: 107207.

[16] Lakzian E, Yazdani S, Lee B J. Passive control optimization of condensation flow in steam turbine blades[J]. International Journal of Mechanical Sciences, 2023, 237: 107804.

[17] Lakzian E, Yazdani S, Mobini R, et al. Investigation of the effect of water droplet injection on condensation flow of different nozzles geometry[J]. The European Physical Journal Plus, 2022, 137(5): 613.

[18] LIU J, LIN Z, WEN X, TIAN G. Recent advances in the technology of moisture removal in steam turbines [J]. Journal of Engineering for Thermal Energy and Power, 2005, 20(1), 1-5.

[19] WANG X, LIAO G, ZHU D, YAO J, BAI X, WANG Z. Numerical simulation on suction performance of steam turbine hollow stationary blade [J]. Turbine Technology, 2012, (3), 195-197.

[20] LI L, WU X, YANG J, FENG Z. Effects of location, shape and width of a suction slot on the water removal performance of a hollow stator blade [J]. Proceedings of the Institution of Mechanical Engineers, Part A: Journal of Power and Energy, 2018, 232(5): 461-72.

[21] WANG S, LIU J. Research on the steam turbine air film heating dehumidification technology [C]. Proceedings of the 2007 Annual Conference of the Turbomachinery, 2007.

[22] YAZDANI S, LAKZIAN E. Numerical simulation and passive control of condensing flow through turbine blade by NVD Method Using Eulerian–Lagrangian Model [J]. Computers & Mathematics with Applications, 2020, 80(1): 140-60.

[23] ZHANG G, ZHANG X, WANG F, WANG D, JIN Z, ZHOU Z. Design and optimization of novel dehumidification strategies based on modified nucleation model in three-dimensional cascade [J]. Energy, 2019, 187: 115982.

[24] Salimi J, Teymourtash A R, Aghdasi M R, et al. Optimization of the surface heating for a stationary cascade turbine blade in wet steam flow[J]. Thermal Science and Engineering Progress, 2023, 39: 101751.

[25] ZHAO Z. Numerical simulation on effects of trailing edge slot blowing on the turbine stator flow field [J]. Turbine Technology, 2013, (2), 105-107.

[26] ALIABADI M A F, ZHANG G, DYKAS S, LI H. Control of two-phase heat transfer and condensation loss in turbine blade cascade by injection water droplets [J]. Applied Thermal Engineering, 2021, 186: 116541.

[27] XU L, YAN P, HUANG H, HAN W. Effects of hot steam injection from the slot at the trailing edge on turbine nozzle vane flow field [J]. Journal of Thermal Science, 2008, 17(4): 298-304.

[28] CHEN T, XIE D, YANG C, ZHANG H, XIONG Y, DU H, ZHANG J. Application of biologically inspired wavy leading edge in nuclear steam turbine cascade [J]. Chinese Journal of Electrical Engineering, 2018, 12.

[29] Han X, Yuan Y, Zhao Z, et al. Numerical investigation of the wet steam condensation flow characteristics in stator cascade with blade surface heating[J]. Engineering Applications of Computational Fluid Mechanics, 2020, 14(1): 1251-1262.

[30] Yang Y, Peng H, Wen C. A novel dehumidification strategy to reduce liquid fraction and condensation loss in steam turbines[J]. Entropy, 2021, 23(9): 1225.

[31] WU F, XIE D, ZHANG J, ZHANG H, WANG C. Improvement of steam turbine blade foil with biomimetic design and its influence on aerodynamic performance; proceedings of the Turbo Expo: Power for Land, Sea, and Air, F, 2019 [C]. American Society of Mechanical Engineers.

[32] Zhong F. Study on haedening mechanism of superhard diamond surface and its nanohardness evaluation technology [D]. Harbin Institute of Technology, 2018.

[33] FIELD J. The mechanical and strength properties of diamond [J]. Reports on Progress in Physics, 2012, 75(12): 126505.

[34] NIE A, BU Y, LI P, ZHANG Y, JIN T, LIU J, SU Z, WANG Y, HE J, LIU Z. Approaching diamond's theoretical elasticity and strength limits [J]. Nature Communications, 2019, 10(1): 1-7.

[35] WANG Y, SHI F, OHFUJI H, GASC J, NISHIYAMA N, YU T, OFFICER T, SHINMEI T, IRIFUNE T. Strength and plastic deformation of polycrystalline diamond composites [J]. High Pressure Research, 2020, 40(1): 35-53.

[36] JING X, ZHU G. Porous aromatic frameworks derived from tetrahedral units [J]. Science Bulletin, 2018, 22.

[37] MOORE M. Predicting the fog-drop size in wet-steam turbines [J]. Wet steam, 1973.

[38] BAKHTAR F, RYLEY D, TUBMAN K, YOUNG J. Nucleation studies in flowing high-pressure steam [J]. Proceedings of the Institution of Mechanical Engineers, 1975, 189(1): 427-36.

[39] BAKHTAR F, ZIDI K. Nucleation phenomena in flowing high-pressure steam: experimental results [J]. Proceedings of the Institution of Mechanical Engineers, Part A: Journal of Power Engineering, 1989, 203(3): 195-200.

- Paper submitted: 12 August 2024
- Paper revised: 05 November 2024
- Paper accepted: 06 November 2024